2012

Magnetic effects of hydride storage in palladium

Jessica Jewett Reed
University of Iowa

MAGNETIC EFFECTS ON HYDRIDE STORAGE IN PALLADIUM

by

Jessica Jewett Reed

A thesis submitted in partial fulfillment
of the requirements for the Master of
Science degree in Chemistry
in the Graduate College of
The University of Iowa

May 2012

Thesis Supervisor: Associate Professor Johna Leddy

Graduate College
The University of Iowa
Iowa City, Iowa

CERTIFICATE OF APPROVAL

MASTER'S THESIS

This is to certify that the Master's thesis of

Jessica Jewett Reed

has been approved by the Examining Committee for the thesis requirement for the Master of Science degree in Chemistry at the May 2012 graduation.

Thesis Committee: _____
Johna Leddy, Thesis Supervisor

_____
Lei Geng

_____
Norb Pienta

To Dad, for instilling the love of science

ACKNOWLEDGMENTS

This work could not have been done without the guidance, support, ingenuity, and caffeination of Dr. Johna Leddy. I am thankful to have such a talented woman as a role model. Also, sincere thanks to group members Krysti Knoche, Garett Lee, Perry Motsegood, and Tim Paschkewitz for their advice, support, and laughter. Former group members Dr. Heung Chan Lee and Dr. Shelley Minteer deserve thanks for their prior work and correspondence regarding this project.

To my loving husband, Jordan, thank you for the words of encouragement, motivation, and support. My parents, Jeff and Barb Jewett, deserve much credit for encouraging me to follow my dreams and supporting me along the way. I am very grateful to the rest of my family and friends for all of their love and support.

Finally, grateful thanks to the University of Iowa Department of Chemistry.

TABLE OF CONTENTS

LIST OF TABLES

Table

LIST OF FIGURES

Figure

CHAPTER 1

INTRODUCTION

1.1 Background

Today a large effort is being made by the government and researchers to transition away from an economy dependent on fossil fuels to alternative energies. Not only are alternative fuel sources necessary to relieve the burden of dwindling oil supplies, they are an answer to environmental sustainability woes. While hydrogen may not yet be a commercialized fuel source, it is an attractive energy source for many reasons. Its natural abundance and straight forward synthesis make it a viable alternative to fossil fuels energy sources. In addition, hydrogen can be stored for a long time without significant degradation unlike, unlike stored electrical charge.In principle, hydrogen fueled vehicles could emit only water from their exhaust systems. However, until better and efficient storage systems are created the use of hydrogen as a fuel is a concern of safety.

There are three types of hydrogen storage: gaseous, liquid, and solid state. A major drawback of gaseous and liquid storage is the relatively small amount of hydrogen that may be stored, even under high pressure. The sheer volume of hydrogen needed to give comparable energy density to gasoline is more than can currently be feasibly stored onboard a vehicle [1]. Solid state storage refers to the storage of hydrogen in metal hydrides and other nano structured materials.

Metal hydrides form when hydrogen reacts with a metal or alloy to create a new hydrogen containing product. The reaction can be seen in Equation. 1 where M

represents the metal and H the hydrogen.

$$x\mathrm{M} + \frac{y}{2}\,\mathrm{H}_2 \rightarrow \mathrm{M}_y\mathrm{H}_x \tag{1}$$

Metal hydrides show promise for solid state storage of hydrogen due to their ability to store large amounts of hydrogen in small volumes and their relative stability. Since metal hydrides are typically solids at ambient conditions, they are less volatile than compressed gas or liquid hydrogen, which is an important factor to consider for fuel containment in the event of a crash.

While this type of solid state storage is likely to be most suitable to meet the specifications for onboard vehicle hydrogen fuel storage, it suffers an energetic cost associated with electrochemically driving the hydrogen into and out of the storage material lattice. In addition to energetic costs, the absorption and release of hydrogen in the metal are kinetically rate limited at atmospheric pressure . This means that the release of the hydrogen fuel from the storage material is not on the time scale demanded by consumers. Imagine the inconvenience of waiting hours or days for fuel to dispense to refill the tank of a vehicle. Hydrogen will not be a viable fuel source until these issues are resolved. This work examines magnetic effects on hydride absorption in palladium metal in an effort to decrease the energetic cost of metal hydride formation, increase the kinetics of the reaction, and promote meaningful discoveries for better solid state hydrogen storage.

With many other metal hydrides and alloys making research headlines for solid state storage of hydrogen, one might question why palladium was chosen. While it is true that alloys of magnesium and lithium provide lighter weight and more cost

effective means for hydrogen storage, they do not absorb hydrogen nearly as readily as palladium. As Jerkiewicz describes it, "Pd and Pd-based alloys are known to be excellent absorbers of H" [2]. As a compromise of sorts, many researchers are examining the use of palladium films or particles on the surface of these metals [3].

Hydrogen absorption in palladium metal is not a new idea, however the use of magnets to improve kinetics for electroabsorption of hydrogen is a novel approach. In the mid-1800s, Sir Thomas Graham explored the absorption of hydrogen in various metals including palladium [4]. Since that time, the palladium-hydrogen system has been thoroughly explored, yet in many ways still remains a mystery. The data and model presented herein attempt to provide insight regarding the complex palladium-hydrogen system.

1.2 Electrochemistry of Hydrogen in Palladium Systems

Palladium has an fcc structure with a lattice parameter of 0.3890 at 298 K [5] . As hydrogen absorbs into the (111) face of the metal, the lattice undergoes an isotropic expansion while maintaining its fcc structure. A representation of the the absorption of hydrogen into the palladium lattice can be seen in Figure 1. The absorbed hydrogen atoms can occupy both tetrahedral and octahedral sites within the lattice. For palladium, both underpotential deposited hydrogen (H_{UPD}) and overpotential deposited hydrogen (H_{OPD}) can occur within the same potential window [2].

A proposed mechanism for the formation of the metal hydride is :

$$\mathrm{M} + \mathrm{H}^+ + \mathrm{e} \rightarrow \mathrm{M\text{–}H}_{ads} \tag{2}$$

$$\mathrm{M\text{-}H}_{ads} \rightarrow \mathrm{M\text{-}H}_{abs} \tag{3}$$

This mechanism describes a kinetically driven system in which absorption of hydrogen and creation of the hydride is limited by the formation of the surface adsorbate. Consider the palladium electrode. H^+ ions migrate to the surface of the electrode where an electron transfer occurs, yielding the adsorbed species. Note that the evolution of hydrogen gas at the electrode surface is not included in the mechanism as it is a side reaction not generated by the experiments herein. The kinetics of the absorption process are assumed to be relatively faster than the adsorption process, however, little is known about the actual kinetics of the reaction. The absorption process creates a metal hydride layer at the surface of the metal. In order for the metal hydride layer to grow, hydrogen must continue to diffuse through the metal hydride layer to the interface of fresh palladium metal and the hydride. Fick's first law can be examined to explain what this means kinetically.

Fick's first law states that the negative flux of a species, J, is proportional to the concentration gradient as seen in Equation 4 [6].

$$-J_O(x,t) = D_O \frac{\partial C_O(x,t)}{\partial x} \tag{4}$$

If the absorption of hydrogen to form the hydride layer is considered to be a linear concentration gradient, the derivative can be written as $\frac{\partial C}{\partial x} = \frac{\Delta C}{x}$, where C is the concentration of the hydrogen and x is the thickness of the metal hydride layer.

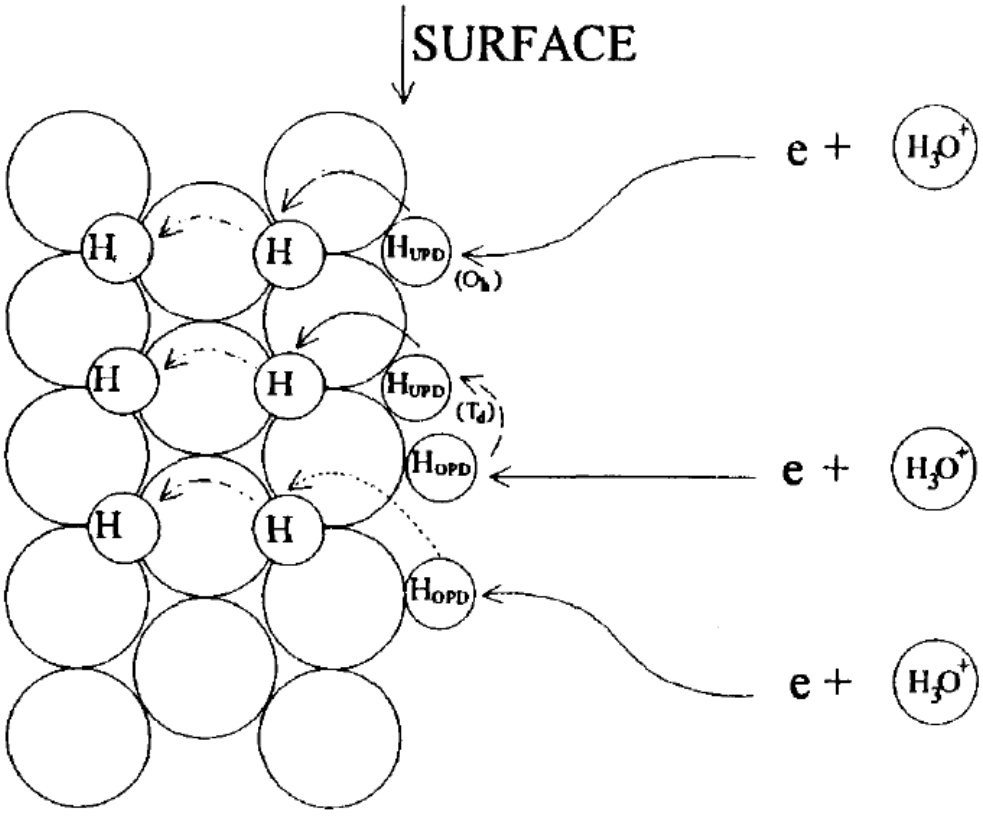

Figure 1. Depiction of hydrogen absorption in palladium. The hydrogen atoms occupy octahedral (O_h) or tetrahedral (T_d) sites in the palladium lattice. Figure is from Jerkiewicz [2].

The growth of the hydride layer, described by the rate expression $\frac{\partial x}{\partial t}$, is directly proportional to the flux of hydrogen through the lattice. Thus, it can be written:

$$\frac{dx}{dt} \sim D\frac{\Delta C}{x} \tag{5}$$

Separation of variables leads to:

$$x\ dx \sim D\ \Delta C\ dt \tag{6}$$

Integration of Equation 6 yields:

$$x \sim \sqrt{Dt} \tag{7}$$

Thus, from Equation 7 it is apparent that the distance the hydride layer grows is proportional to the square root of the reaction time, or that the square root of the distance the film grows is proportional to the reaction time. Therefore, this illustrates the need for smaller dimensions of metal hydride storage materials to reduce the time of such reactions associated with refueling.

Due to the short time scale nature of the cyclic voltammetry experiments in this work, it is reasonable to say that Eqn. 4 is not necessary to explain the hydrogen absorption diffusion kinetics. The hydrogen absorption in these experiments is likely on the order of nano molar concentration, thus the layer of hydride formation is not great enough to be governed by Fick's first law of diffusion. Nonetheless, it is important to note that in larger time scale cases, such as the metal hydride solid-state storage tanks, hydrogen absorption into the metal lattice is governed by this law.

1.3 Cyclic Voltammetry

Cyclic voltammetry (CV) is an electrochemical technique in which current is measured as a potential range is scanned. CV provides unique information about the energetic costs of electroabsorbing hydrogen because the current output at the potential of absorption can be measured. In order to decrease energetic losses associated with electroabsorbing hydrogen, the increased current seen when hydrogen absorbs into the metal needs to occur at a lower potential than the traditional hydride formation potential. The hydrogen absorption occurs on the forward sweep or the reductive wave of the voltammogram.

Gregory Jerkiewicz has done extensive electrochemical research on the palladium and hydrogen system [7]. Figure 2 shows CV data obtained by Jerkiewicz for a bare palladium electrode in 0.5 M H_2SO_4 electrolyte at scan rate 50 mV/s. These data were used as a reference standard for the studies herein. In order to determine that the experimental observations obtained demonstrated the absorption phenomena expected, comparisons between experimental results and the reference voltammogram were made. These comparisons can be found in the Results and Discussion chapter.

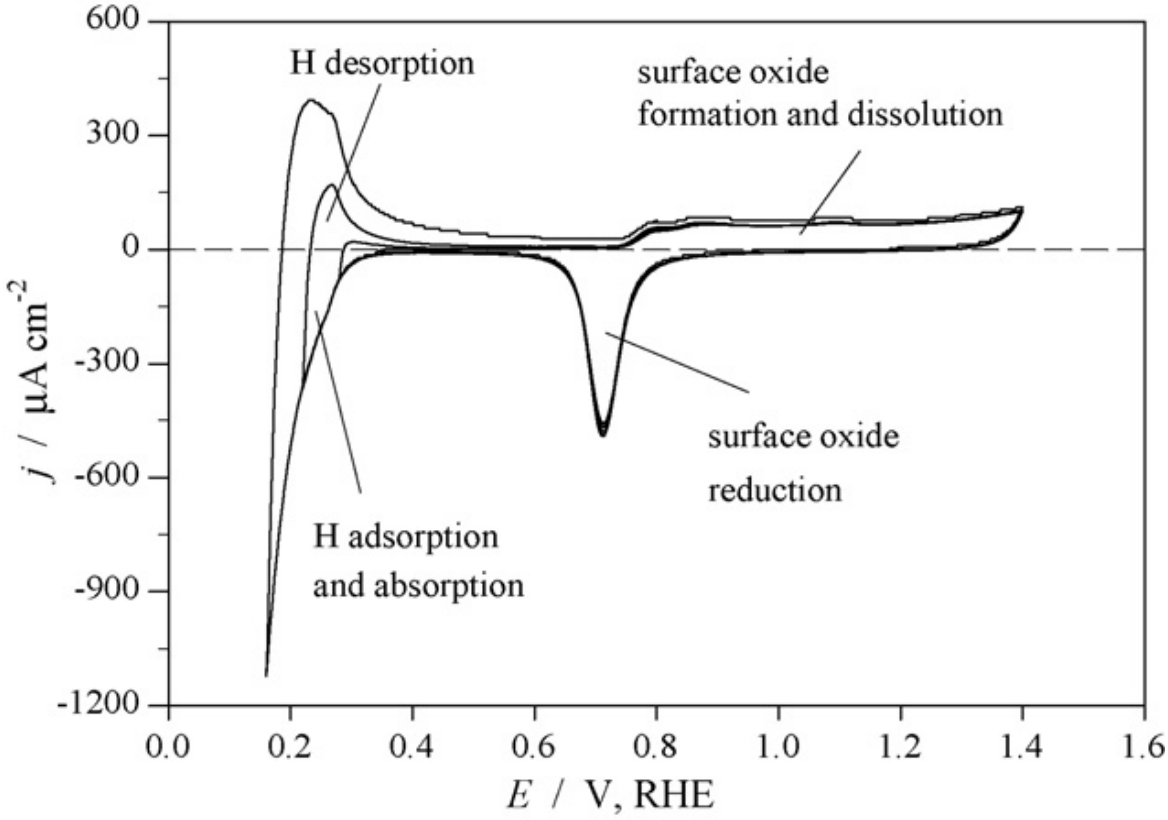

Figure 2. Series of CV scans from Jerkiewicz [7]. A Pd electrode in 0.5 M H_2SO_4 at 298 K. Scan rate is 50 mV/s. The upper potential limit is fixed at 1.40 V while the lower limit is decreased gradually to show H absorption into Pd.

CHAPTER 2

EXPERIMENTAL

The following details the materials and experimental procedures.

2.1 Electrodes and Instrumentation

The electrochemical cell is a three electrode cell. Measurements were made by cyclic voltammetry.

2.1.1 Working Electrode

The working electrode was a Pine Instruments palladium rotating disk electrode (RDE) with a teflon shroud. All experiments were done on this one electrode. The electrode was of geometric area 0.438 cm^2. A detailed cleaning procedure was employed between uses to ensure electrode surface reproducibility. First, the electrode was cleaned with an ethanol soaked Kimwipe to dissolve any remaining polymer deposits. Next, the electrode was polished by hand on a polishing pad with, successively, 3, 1, 0.3, and 0.05 μm grit alumina oxide polishing powders (Buehler) in water slurry. The electrode was rinsed with water between different grits. Finally, the surface is rinsed thoroughly with distilled water and stored upright in a protective cylinder until ready for use .

2.1.2 Counter and Reference Electrodes

The counter electrode consisted of high surface area platinum mesh with a

geometric area of approximately one inch squared. The electrode was cleaned by soaking in concentrated HNO_3 for five minutes and rinsed with distilled water prior to use. A saturated calomel electrode (SCE) with standard potential 0.2412 V vs. NHE served as the reference electrode. The SCE was cleaned by a brief rinse with distilled water prior to use and blotted dry with a Kimwipe.

2.1.3 Voltammetry

A CHI 1030 potentiostat from CH Instruments, Inc. was used to collect all cyclic voltammetric data. Voltammograms were typically recorded at various scan rates between 25 to 150 mV/s. The scans were taken with scan rate order randomized to eliminate scan rate bias and possible changes associated with extra electrochemical events. To be consistent with literature data, scans were commonly taken at a scan rate of 50 mV/s. The electrolyte and pH varied and are noted in each case. Common electrolytes were 0.1 M $NaNO_3$ (Fisher) and 1.0 mM HNO_3 (Fisher). Electrolyte solutions were purged with nitrogen gas for 15 minutes before experimental tests. All experiments were conducted at room temperature. Voltammetric data were analyzed by macros in Microsoft Excel created by group member Tim Paschkewitz.

2.2 Magnetic Particles

Magnetic microparticles were obtained from several sources. The most effective microparticles were coated magnetite microparticles, SiMAG®, from commercial distributor Chemicell (Germany). The particles consist of a single core of magnetite (Fe_3O_4) encapusulated in a thin silane coat The silane coat makes the magnetite

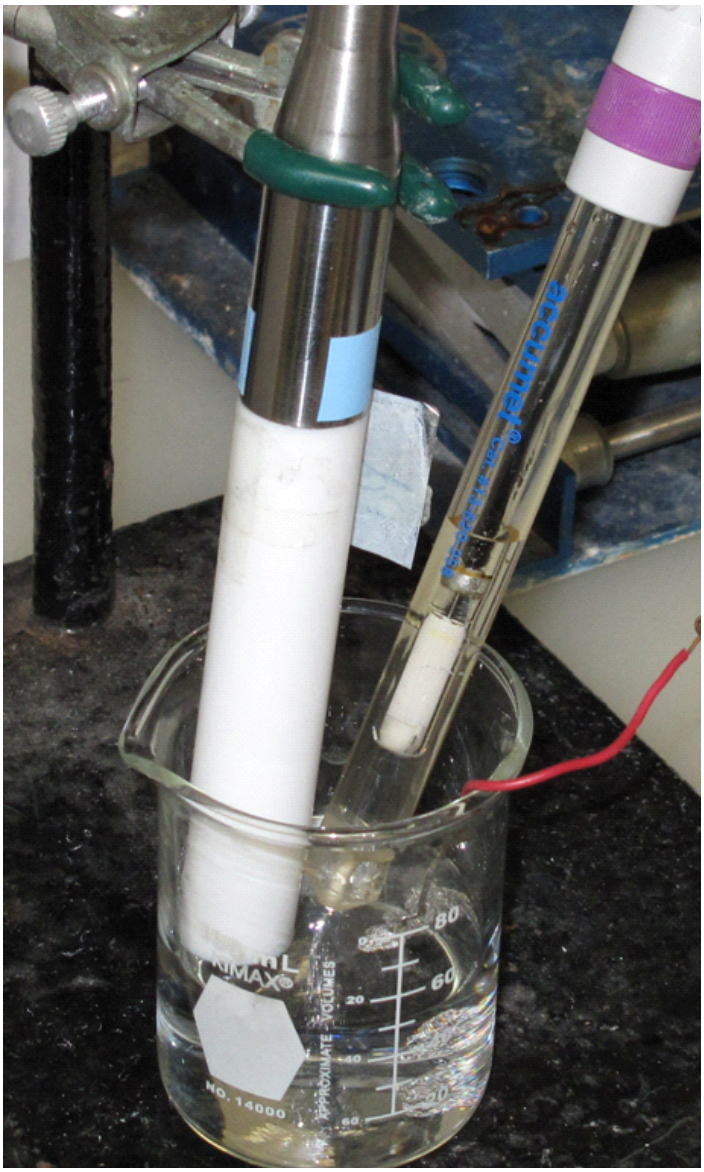

Figure 3. The electrochemical cell. The Pd working electrode is in the circular cross section of the electrode that has a white shaft, whereas the SCE reference electrode has a white and purple top. The Pt mesh counter electrode is attached to the red wire and is visible in the bottom of the beaker.

Table 1. Properties and naming of commercial Chemicell magnetite particles.

Commercial Name	**Functional Group Coating**	**Short Name**
SiMAG-Methyl	-Si-CH_3	C1
SiMAG-Propyl	-Si-$(CH_2)_2CH_3$	C3
SiMAG-Octyl	-Si-$(CH_2)_7CH_3$	C8
SiMAG-Octadecyl	-Si-$(CH_2)_{17}CH_3$	C18

chemically inert but is sufficiently thin to establish a magnetic field at the electrode surface.These particles have different chain length in the silane surface coatings and are named as C_n for -Si-$(CH_2)_{n-1}CH_3$ silane coatings. The names are listed in Table 1. The particles are identified by their short name throughout this work.

Properties in common for the SiMAG particles regardless of silane chain length include average size of 1μm, surface area of approximately 100 m^2/g, and density of 2.25 g/cm^3. Also, the number of particles is constant at 1.8 x 10^{12}/g.

Former lab member Heung Chan Lee determined the magnetic susceptibility of the commercial SiMAG particles from Chemicell. His dissertation describes the experiment for determining the volume magnetic susceptibility [8]. His findings are summarized in Table 2. It is of note that the expected pattern of increasing chain length of coating decreasing the magnetic field strength is not consistently observed. The C18 particles have higher magnetic field strength measurements than C8 particles. Otherwise, the shorter chain lengths have stronger magnetic fields.

Other microparticles included polymer magnetite composites from Bangs Laboratories, Inc. (ProMag PMC3N). These particles have an average size of 2.70 μm and density of approximately 1.22 g/cm^3. Based on density, the magnetic content is less than the Chemicell particles.

Table 2. Volume magnetic susceptibilities in centimeter-gram-second units for SiMAG particles as determined by Lee.

	Volume magnetic susceptibility (c.g.s.)
C1	5.39×10^{-5}
C3	2.39×10^{-5}
C8	8.60×10^{-6}
C18	1.96×10^{-5}
water	-1.06×10^{-6}

The $SmCo_5$ (Alfa) particles are not coated. Fellow group member Garett Lee used a magnetic susceptibility balance to determine the volume magnetic susceptibility values. The $SmCo_5$ particles have magnetic susceptibility of 1.11 x 10^{-1} c.g.s.

2.3 Nafion and Nafion Composite Modified Electrode

One of the ion exchange polymer coatings used in these experiments was Nafion®. Developed by scientists at DuPont, Nafion consists of a Teflon-like fluorocarbon backbone with side chains that terminate in sulfonic acid sites [9]. The chemical structure of Nafion is:

$$\left[\left[(CF_2CF_2)_n\text{-}CF_2\underset{\displaystyle (OCF_2\underset{\displaystyle CF_3}{\underset{|}{CF}}-)_m OCF_2CF_2SO_3H}{\underset{|}{CF}}\text{-} \right] \right]_x$$

where m is usually 1; $5 \leq n \leq 7$

The proton from the sulfonic acid group can easily exchange cationic species from solution, including other protons from solution, such as HNO_3. Nafion, an ion conducting polymer, serves as a membrane film with high proton concentration between the electrode and electrolyte solution. Nafion is used to support micromagnets on the electrode surface. Thus, simple Nafion films serve as controls

for the magnetic composite films. Prior studies have shown that Nafion films and Nafion films with low loading of polystyrene particles ($\leq$ 5 %) have the same cyclic voltammetric response [10]. In general, addition of nonmagnetic microparticles either yields the same cyclic voltammetric response as simple Nafion films or occasionally degrades performance relative to Nafion.

2.3.1 Preparation of Nafion and Composite Films

The Nafion films cast on the electrode are prepared from a commercial Nafion suspension (Ion Power, Inc.). The commercial suspension is 5% weight Nafion in a mixture of alcohols and water. The palladium working electrode is modified with either (a) a Nafion film; (b) a composite of Nafion and magnetic microparticles with no external magnetic field applied; or (c) a composite of Nafion and magnetic microparticles formed under an external magnetic field. All composites are 15% wt/wt magnetic particles.

The simple Nafion film preparation consists of depositing 5 μL of the Nafion suspension on the surface of the electrode via pipette.

Composite films require only slightly more effort to prepare. The Nafion suspension and microparticles are mixed in a centrifuge tube and then vortexed briefly to suspend microparticles. The suspension is used immediately to form composite modified electrodes. In composite cases, a 5 μL aliquot of Nafion and magnetic microparticles is applied to the electrode. When composites are aligned in the magnetic field, a NdFeB ring magnet encompassing the electrode surface is used. The ring magnet has outer diameter of 7.5 cm, inner diameter of 5 cm,

and height of 1cm.To magnetize the composite, the electrode modified by the suspension is centered inside a hollow cylinder and magnet as shown in Figure 4. The field strength of the external magnet is sufficient to magnetize and align the microparticles. Once magnetized by an external field, the microparticles are able to sustain that magnetic field. Without magnetization by the external magnet, the microparticles may sustain a residual magnetic field. No attempt to demagnetize microparticles was made.

In all cases, the modified electrode was air dried in an upright position for 30 minutes before being placed in a vacuum desiccator to ensure complete evaporation of solvent. Vacuum drying times varied for composite and Nafion films. Interactions between the magnetic particles and the Nafion shorten the useable lifetime of the composite if the film is dried too long. Composite films are dried for 50 minutes whereas simple Nafion films are dried for upwards of 2 hours.

2.4 TMODA and TMODA Composite Modified Electrode

A modified Nafion suspension, octadecyltrimethylammonium bromide (TMODA, Sigma) Nafion, was employed as a less harsh alternative to pure Nafion.

2.4.1 TMODA Chemistry and Preparation

The TMODA solution was prepared in the laboratory by Tim Paschkewitz, a fellow group member, following the procedure outlined by Minteer [11]. TMODA Nafion is formed by exchanging the proton of Nafion with the TMODA cation. The

TMODA modified Nafion has a lower ion exchange capacity because the film volume increases and is less acidic than a pure Nafion film.The milder environment is less likely to dissolve the magnetic microparticles and their coatings than the highly acidic proton exchanged Nafion.

2.4.2 Preparation of TMODA and Composite Films

The TMODA films cast on the electrode are prepared from TMODA modified Nafion. Prior to use, the suspension is vortexed approximately 15 seconds to ensure effective mixing of the Nafion and TMODA. The palladium working electrode was modified with either (a) a TMODA film; (b) a composite of TMODA and magnetic microparticles with no external magnetic field applied; (c) a composite of TMODA and magnetic microparticles formed under an external magnetic field; or (d) a composite of TMODA and 3 to 10 μm glass beads with density 2.5 g/cm^3 (Polysciences, Inc.).

The simple TMODA film was prepared by depositing 5 μL of the TMODA suspension on the surface of the electrode with a pipette.

In composite cases, a 5 μL aliquot of TMODA and magnetic microparticles is applied to the electrode The composite mixture was 50 mg microparticles per mL suspension. The composite suspensions were vortexed briefly to suspend microparticles prior to use and were refrigerated when not in use. A NdFeB ring magnet was used for magnetic field alignment (Figure 4).

In each case, the modified electrode was air dried in an upright position for 30 minutes prior to being placed in a vacuum desiccator. All TMODA films were dried

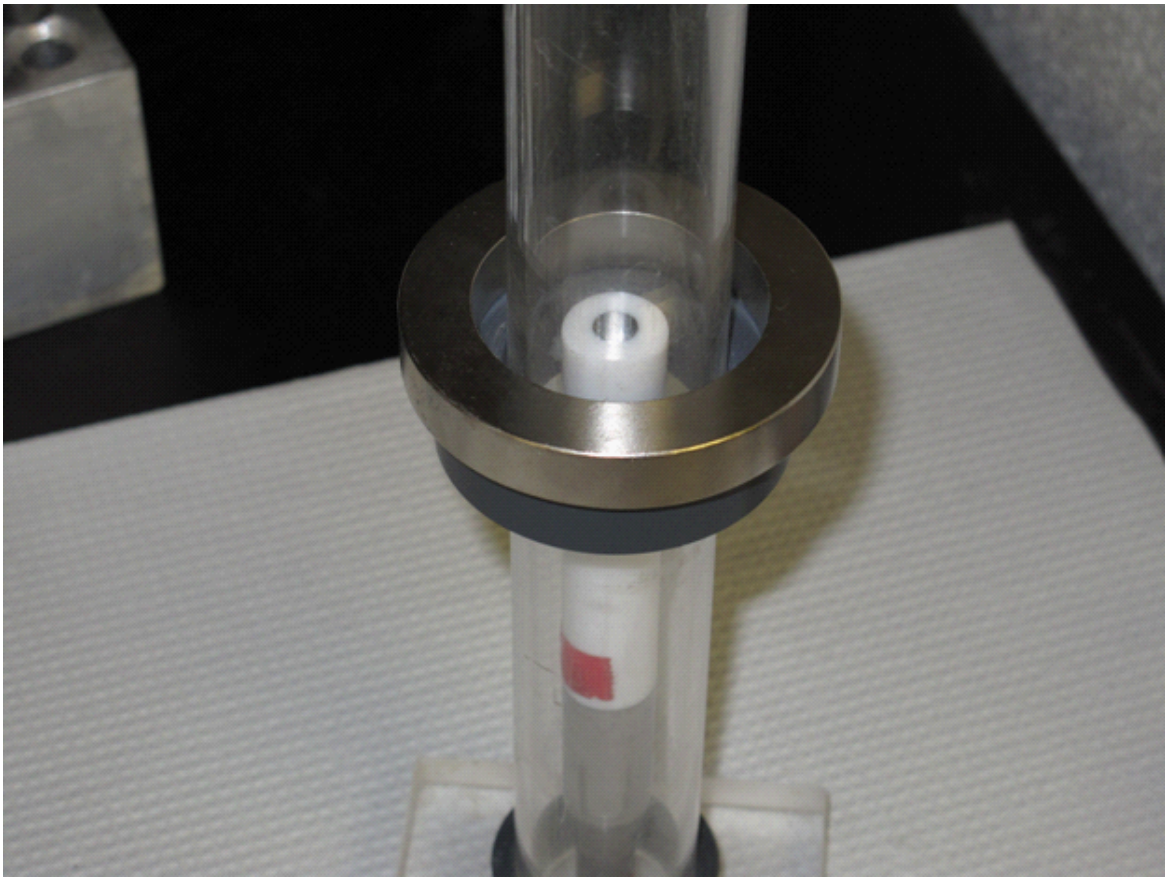

Figure 4. The modified electrode surface air dries in an upright position within the magnetic field of a NdFeB ring magnet.

in a vacuum desiccator for 50 minutes.

The density of TMODA is not readily determined and varies with preparation of each new batch of TMODA modified Nafion, thus film thicknesses for TMODA and composite films are unknown. It is assumed that thicknesses are comparable to those of the Nafion films.

CHAPTER 3

RESULTS AND DISCUSSION

3.1 Nafion Films and Composites

3.1.1 Comparison to literature studies

In order to verify the response seen from the reductive wave as actual hydrogen absorption, the bare palladium electrode was tested in acidic solution. Figure 5 shows a voltammetric profile for the bare, unmodified Pd electrode in 0.1 M HNO_3 at scan rate of 50 mV/s.

The results seen on the bare electrode are similar to that of the bare electrode in sulfuric acid as witnessed by Jerkiewicz. The reductive wave in shows a reduction of surface oxides followed by steep take off of the hydride absorption. The oxidative wave shows a large peak around 0 V corresponding to the desorption of hydrogen.

3.1.2 Composite Films of Nafion and Magnetic Particles

Initial tests of composite Nafion films were done with Bangs PMC3N magnetic microparticles. The composite film was dried within the field of a NdFeB ring magnet. An overlay of voltammetric data comparing the blank Nafion film with the composite can be seen in Figure 6. The magnetic particles show enhanced current output at lower overpotential during the absorption process. It is unclear

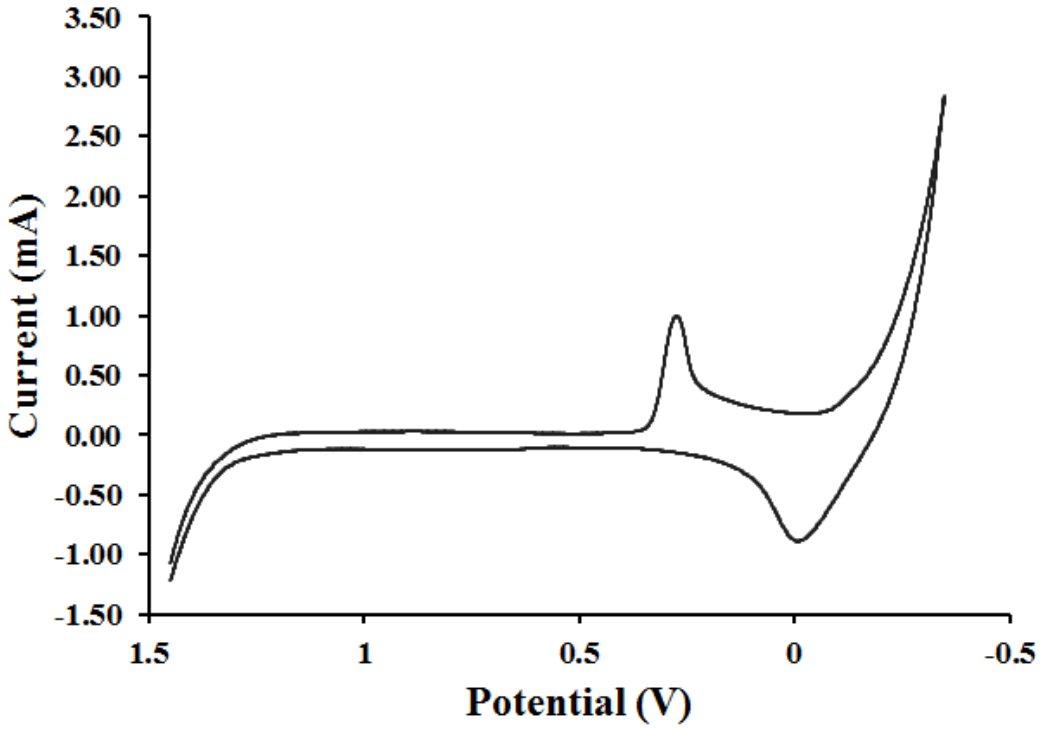

Figure 5. Voltammetric profile for bare, unmodified Pd electrode versus SCE in 0.1 M HNO_3. Scan rate of 50 mV/s.

as to why the desorptive wave is so much larger for the blank Nafion film than for the composite. The acidity of Nafion was not ideal for the polymer coated Bangs microparticles, thus they were not used in further experiments.

Nafion was also tested with $SmCo_5$ magnetic microparticles. The composite film was not magnetized in an external field. There does not appear to be any effect with the magnetically modified film. This could be because that it was very difficult to get the $SmCo_5$ particles to disperse in the Nafion suspension, even with sonication.

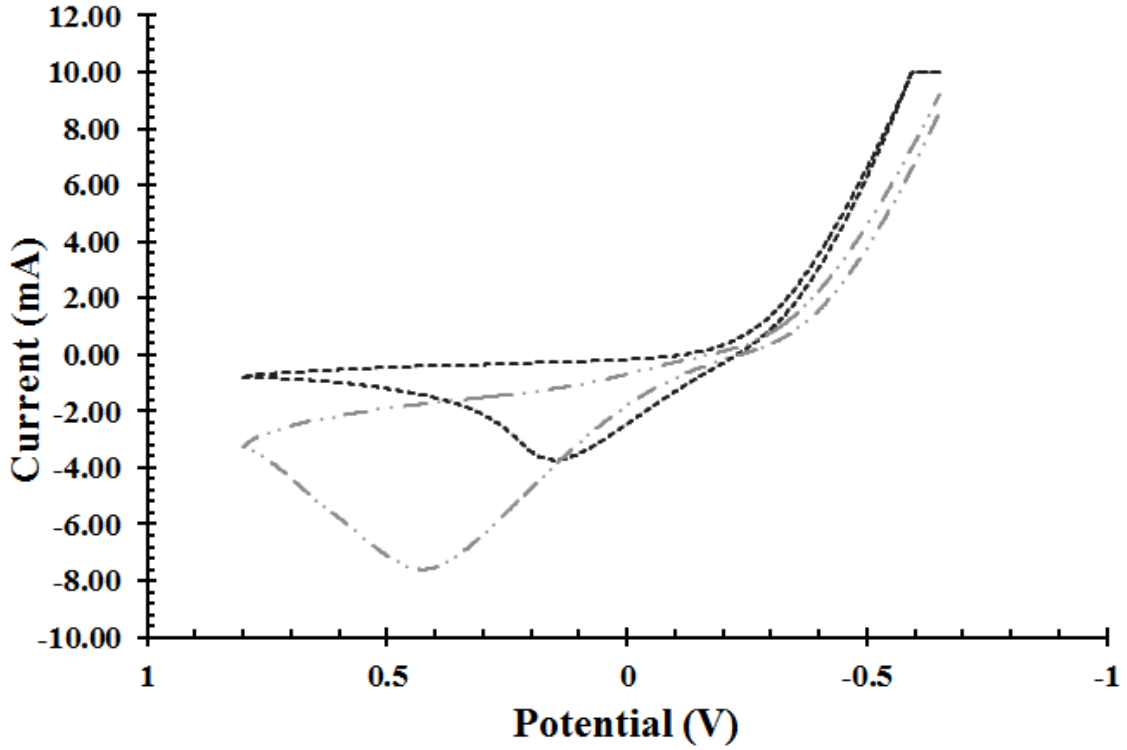

Figure 6. Comparison of voltammetric data for blank Nafion and for a composite of Nafion and Bangs magnetic microparticles in 0.1 M HNO_3 at scan rate of 50 mV/s. The film was dried in an external magnetic field. Blank Nafion film (gray, long-short dash) and composite (black, short dash) are shown. The voltammetric wave for the magnetically modified electrode is characteristic of faster kinetics than the simple Nafion film.

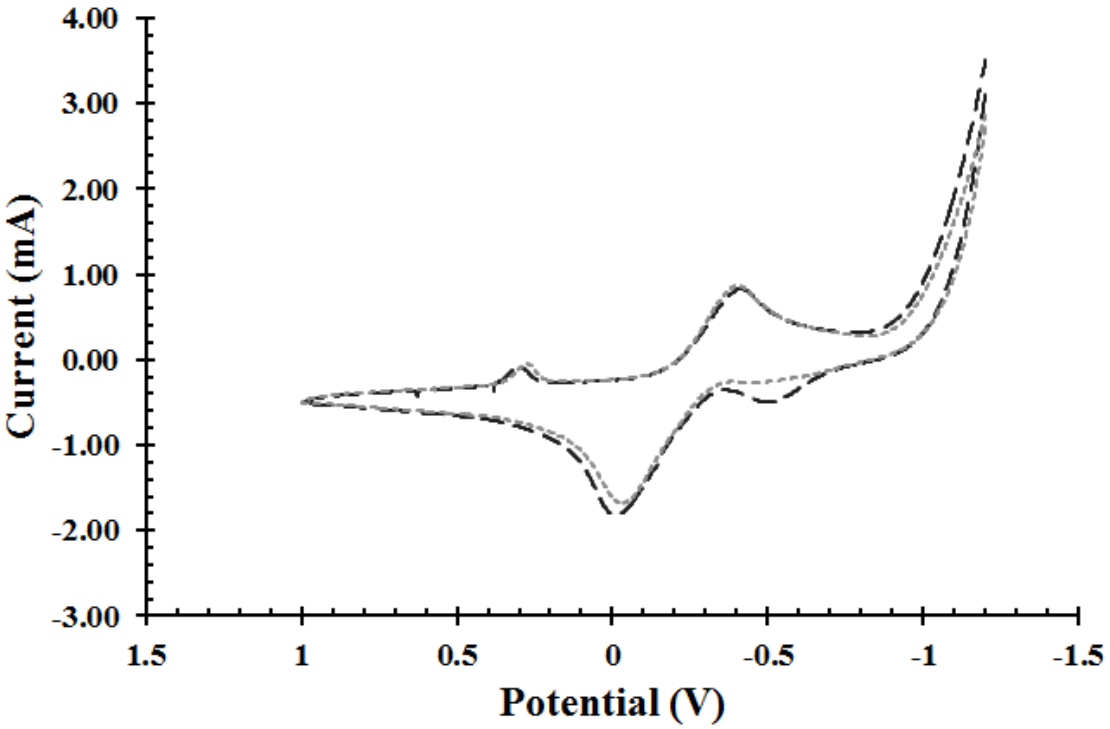

Figure 7. CV overlay of blank TMODA and composite of TMODA and $SmCo_5$ at 50 mV/s scan rate. $SmCo_5$ (black, long dash), Blank TMODA (gray, short dash).

Also, the $SmCo_5$ particles are uncoated, leaving them vulnerable to oxidation, and ultimately loss of magnetic properties, in the acidic Nafion. Dissolution of the particles was visibly noticeable after completion of the experiments. Any future work with uncoated $SmCo_5$ particles should evaluate particles processed by grinding or ball milling prior to suspension in Nafion.

3.2 TMODA Results

The following details the results of the composite films made with TMODA.

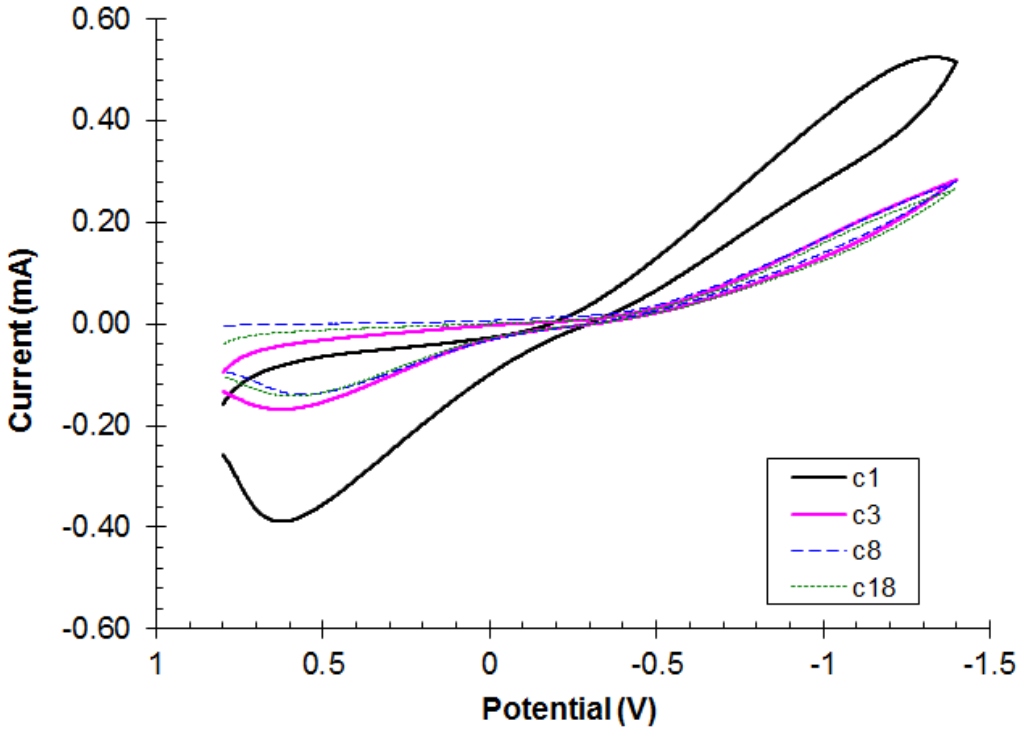

Figure 8. An overlay of cyclic voltammograms from composite films of TMODA and SiMAG particles. The electrolyte is 1.0 mM HNO_3 and scan rate is 50 mV/s. C1(black, solid), C3 (pink, solid), C8 (blue, long dash), C18(green, short dash).

3.2.1 SiMAG Particles

The SiMAG particles were the only magnetic microparticles used in composites with TMODA because of their strong field strength and acid resistant silane coating.

Figure 8 displays the cyclic voltammogram overlay of the SiMAG particles and TMODA composite in 1.0 mM HNO_3 electrolyte with scan rate of 50 mV/s. It is apparent that the C1 particles show greater current gains compared to the other SiMAG particles. This is likely due to the short silane chain length of the particle coating. Therefore, C1 particles were the choice magnetic particles for remaining

Table 3. Current output based on magnetic particle type in the film at -1.0 V potential during the reductive scan.

SiMAG Particle in Film	**Current (mA) at -1.0 V**
C1	0.41
C3	0.17
C8	0.17
C18	0.16

trials.

The current output based on SiMAG particle type in the composite at -1.0 V potential during hydrogen absorption is shown in Table 3. At this arbitrary potential it is clear that C1 magnetic microparticles outperform the other SiMAG magnetic particles by nearly three times the current output.

To confirm that the effect of increased current at a lesser potential was due exclusively to the magnetic property of the particles, and not general particulate matter effects in the film, a composite film of TMODA containing glass microbeads was cast and tested in 1.0 mM HNO_3 electrolyte. Figure 9 shows an overlay of the CV data obtained for a blank TMODA film, a composite of TMODA and C1, and a composite of TMODA and glass microbeads. The glass microbeads showed similar performance to that of the blank thus confirming that the increased current observed is due solely to the presence of the magnetic microparticles and not to general particulate species.

The question arose as to whether field alignment of the magnetic microparticles had any influence on current gains. Figure 10 displays an overlay of cyclic voltammograms of blank TMODA, and composites containing C1 microparticles that are either magnetized or non-magnetized. The magnetized composite film was

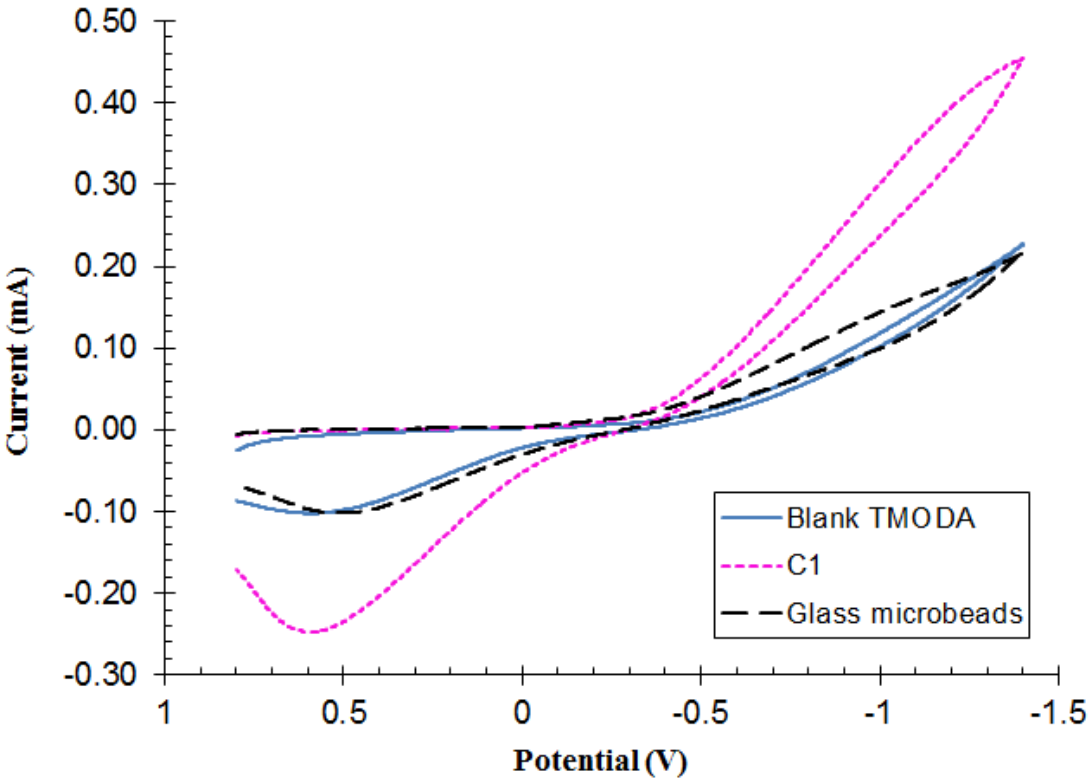

Figure 9. Overlay comparing CV data for a blank TMODA film, and composites of TMODA with C1 or glass microbeads. The electrolyte is 1.0 mM HNO_3 and scan rate is 50 mV/s. Blank (blue, solid), C1 (pink, short dash), Glass microbeads (black, long dash).

Table 4. Current output based on film composition at -1.0 V potential during the reductive scan.

Film Composition	**Current (mA) at -1.0 V**
Blank TMODA	0.12
Magnetized C1 particles in TMODA	0.22
Non-magnetized C1 particles in TMODA	0.32

exposed to an external magnetic field while drying. It is apparent that the non-magnetized composite outperforms the magnetized version. Table 4 displays data describing the current output at -1.0 V on the reductive wave. The nonmagnetized C1 particles outperform the magnetized C1 particles with approximately 1.5 times more current at the same overpotential. The composite films both outperform the blank TMODA film, but the nonmagnetized C1 particles provide 2.7 times more current output than the blank, whereas the magnetized C1 particles provide 1.8 times more current. This raises the question as to why not externally magnetizing the microparticles shows greater current gains than the magnetized particles. This is likely due to a better distribution of the magnetic field on the surface of the electrode in the nonmagnetized case where the particles have a residual magnetic field. Placing the electrode in an external magnetic field to magnetize the microparticles causes the particles to align and form pylons on the electrode surface. This causes a less well distributed magnetic field on the electrode surface.

3.2.1.1 pH Effects

The effect of pH was studied in order to determine how the system responds to changes in the concentration of H^+ in solution.

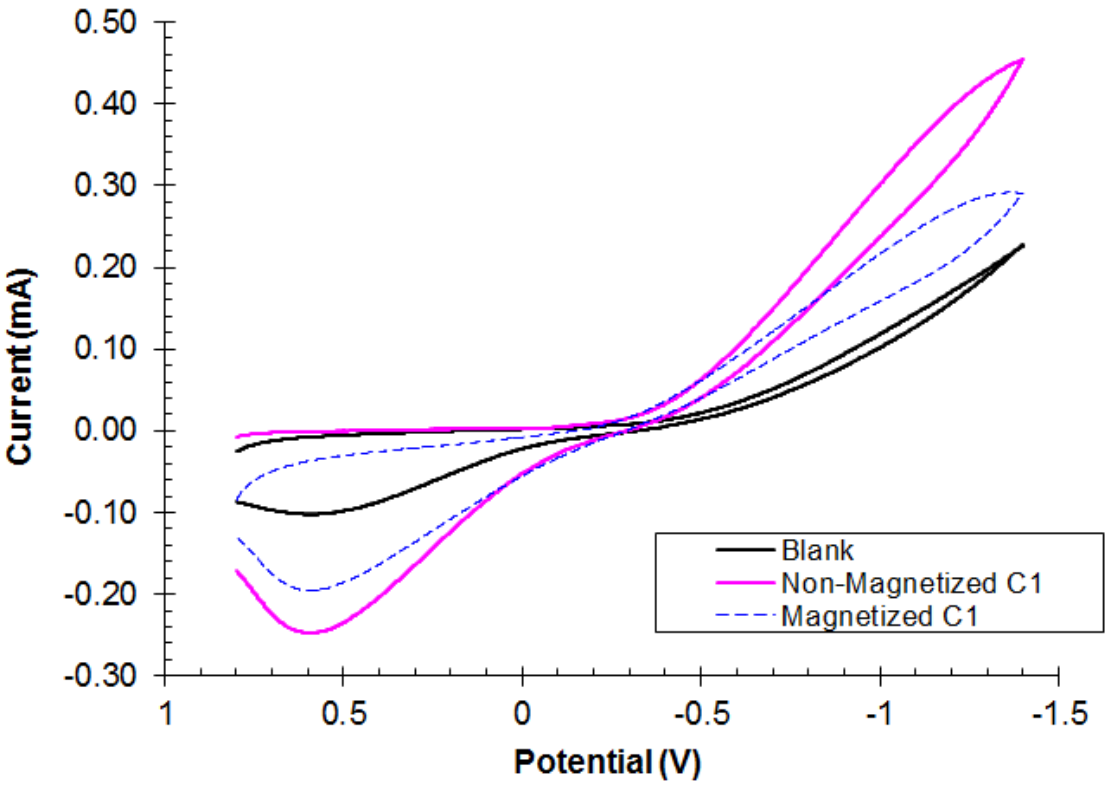

Figure 10. An overlay of CV data comparing blank TMODA to composites containing C1 microparticles. The magnetized C1 particles had been exposed to an external magnet for magnetic field alignment. The supporting electrolyte is 0.1M HNO_3 and scan rate is 50 mV/s. Blank (black, solid), Non-magnetized C1 (pink, solid), Magnetized C1 (blue, short dash).

Table 5. Current output based on film composition and pH of electrolyte at -1.0 V potential during the reductive scan.

Film Composition	**Current (mA) at -1.0 V**
Blank TMODA, pH 5	0.11
Blank TMODA, pH 10	0.082
C1 particles in TMODA, pH 5	0.19
C1 particles in TMODA, pH 10	0.12

The location of the hydride desorption peak was not well defined in supporting literature, causing uncertainty about the large broad peak occurring on the oxidative wave. To verify that this peak is that of hydride desorption, the C1 and TMODA composite film was tested in 1.0 M $NaNO_3$ electrolyte at pH 5.16 and pH 10.01. NaOH was added to the electrolyte solution to achieve pH 10.01. An increase in pH caused a decrease in the oxidative wave, indicative of lower H^+ ion concentration rather than an oxide stripping wave. The blank TMODA film was also tested in the 1.0 mM $NaNO_3$ electrolyte at pH 10. Figure 11 shows an overlay of the CV data collected at pH 5 and pH 10.

Examination of Figure 11 reveals that the blank TMODA electrode in pH 5 electrolyte performs similarly to the composite film in pH 10. Thus, it takes five orders of magnitude decrease in the concentration of H^+ for the magnetic microparticles to give current output comparable to an electrode without magnets. The absorption take-off peak in the reductive scan for C1 at pH 5 occurs several hundred millivolts before that of the blank films. The blank TMODA film modified electrodes can be thought of as the traditional palladium hydride sytem. Therefore, by adding magnetic microparticles to the traditional palladium hydride system, the potential required to electrochemically absorb hydrogen is decreased.

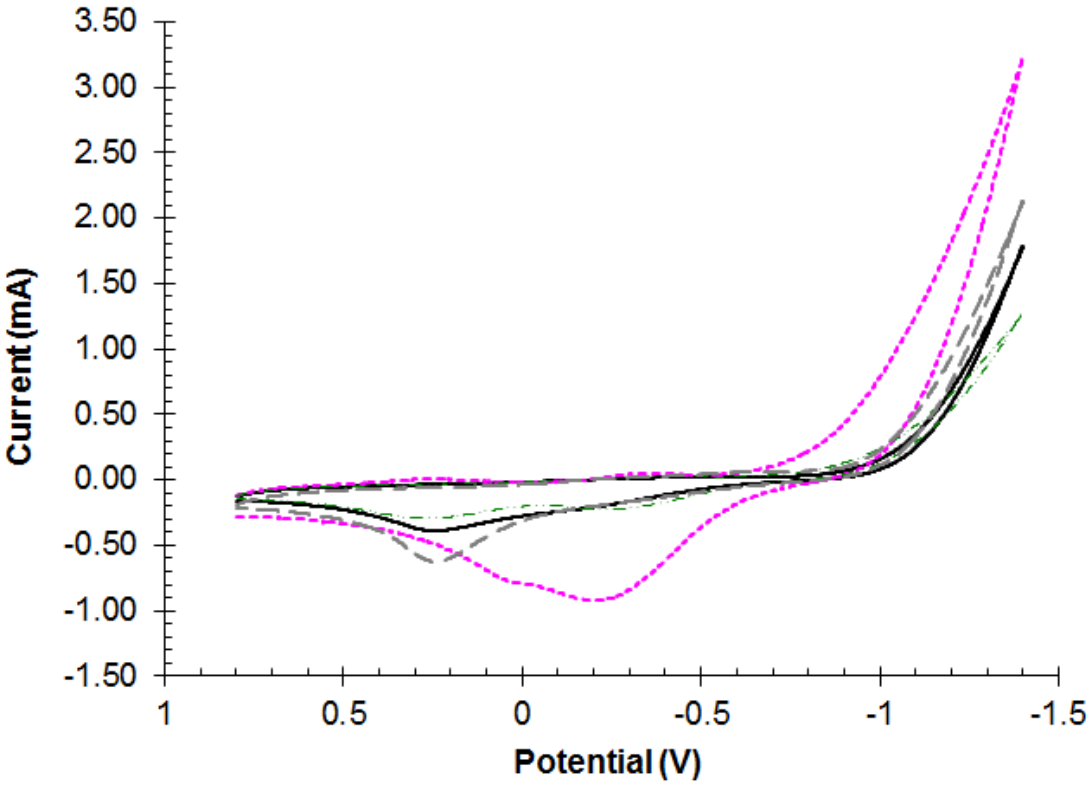

Figure 11. An overlay of cyclic voltammogram data for blank TMODA, and composite films of TMODA and C1 particles at pH values of 5 and 10. The electrolyte was 0.1 M $NaNO_3$ and the scan rate was 50 mV/s. Blank TMODA at pH 10 (black, solid), Blank TMODA at pH 5(gray, long dash), C1 at pH 5 (pink, short dash), C1 at pH 10 (green, long dash- short dash).

Table 5 displays the current output for the blank films and composite films at pH values of 5 and 10. The blank TMODA films perform similarly regardless of H^+ concentration. The magnetic C1 microparticles give nearly twice as much current output as the blank film in pH 5 solution, thus indicating that the magnetic particles are inducing the increased current output This means that the absorption rate of hydrogen into the metal is increased by adding magnetic microparticles to the surface of the electrode.

3.3 A Model for Metal Hydride Formation in the Absence of Hydrogen Evolution

Consider a simple model for metal hydride adsorption. The system is a solution that contains proton, H^+, in solution at a concentration c^*. The electrode is a large flat metal surface, M where M is only the surface sites at the solution metal interface. The mechanism, according to Jerkiewicz , is that the proton in solution H^+ immediately at the electrode M surface undergoes a one electron e reduction to form adsorbed hydrogen radical ($H^\bullet$) [2]. In Jerkiewicz's version, there is no intermediate step and the $H^\bullet$ is immediately *adsorbed* as MH_{ads} in a concerted reaction at a formal potential $E^{0'}$.

$$M + e + H^+ \underset{k_b}{\overset{k_f}{\rightleftarrows}} MH_{ads} \tag{8}$$

MH_{ads} species are surface species. This reaction is followed by a step in which the metal surface *adsorbed* hydrogen radical is *absorbed* into the bulk metal. The absorption leaves a metal site free on the surface and a hydride free in the bulk

metal.

$$MH_{ads} \underset{k_{-1}}{\overset{k_1}{\rightleftarrows}} M + H^{\bullet}_{abs} \tag{9}$$

Consider some features of the model developed by Lasia and Grégoire, where essentially the proton is taken as being in excess concentration; no proton concentration is included in their equations such that the proton in solution is effectively pseudo first order [12]. Lasia and Grégoire's equations are developed in terms of the surface concentration of M and MH_{ads} and do not include the proton concentration.

In the context where the proton concentration is sufficient that it does not limit the rate, the electrode surface is composed of two sites, active sites for adsorption where there is no adsorbate, M, and the sites that are blocked by adsorbed hydride, MH_{ads}. There are no other allowed sites and no other allowed adsorbates. The total number of available surface sites, Γ^* (moles/cm^2), accounts for the surface coverage of the reactive sites Γ_M and the blocked sites $\Gamma_{MH_{ads}}$ such that

$$\Gamma^* = \Gamma_M + \Gamma_{MH_{ads}} \tag{10}$$

Division by Γ^* yields fractional concentrations, where $\theta_M = \Gamma_M/\Gamma^*$ and $\theta_{MH_{ads}} = \Gamma_{MH_{ads}}/\Gamma^*$.

$$1 = \theta_M + \theta_{MH_{ads}} \tag{11}$$

Several assumptions are now introduced.

First, the reaction rate at the surface is sufficiently slow as compared to mass transport in the solution that concentration of proton H^+ at the electrode surface is the same as bulk, c^*. Thus, mass transport in solution is not a parameter in

determining the rate. Also, the rate expressions are pseudo first order in proton concentration in solution.

Second, the amount of $H^{\bullet}_{abs}$ generated on the time scale for the voltammetric perturbation is small and that once the $H^{\bullet}_{abs}$ is deployed in the bulk metal, the metal serves as an infinite sink for absorbed hydride. It is also assumed that transport of the small amount of hydride in the bulk metal sufficiently rapid so as not to impact the reaction rate. Thus, mass transport in the bulk metal for the absorbed hydride $H^{\bullet}_{abs}$ is not rate determining and is therefore not included in the model. Also, the concentration of the absorbed hydride in the bulk metal does not change significantly during a cyclic voltammetric sweep, and is therefore constant and so the rates are pseudo first order in absorbed hydrogen concentration for cyclic voltammetric experiments.

The current measured for the system is governed by Butler Volmer kinetics for Equation 8. For pseudo first order in proton in solution and the Butler Volmer expressed in fractional surface coverage,

$$\frac{i\left(E\right)}{FA\Gamma^{*}/\delta} = k_{f}\left(E\right)\theta_{M}\left(E\right) - k_{b}\left(E\right)\theta_{MH_{ads}}\left(E\right) \tag{12}$$

where Γ^{*}/δ has units of concentration when δ is the thickness of the reaction layer, perhaps the thickness of the proton layer in solution at the surface of the electrode where the hydrated size of ~ 1 nm is an estimate. This leaves the heterogenous rate constants in the correct cm/s units. For Butler Volmer, the potential dependence of

the heterogeneous rate constants is

$$k_f(E) = k^0 \exp\left[-\frac{\alpha F}{RT}\left(E - E^{0'}\right)\right] \tag{13}$$

$$k_b(E) = k^0 \exp\left[\frac{(1-\alpha) F}{RT}\left(E - E^{0'}\right)\right] \tag{14}$$

Note that because of Equation 11, Equation 12 is equivalently written in terms of the hydride surface coverage as

$$\frac{i(E)}{FA\Gamma^*/\delta} = k_f(E)\left[1 - \theta_{MH_{ads}}(E)\right] - k_b(E)\,\theta_{MH_{ads}}(E) \tag{15}$$

For Equations 8 and 9, the rate expressions for θ_M and $\theta_{MH_{ads}}$ are

$$\frac{d\theta_{MH_{ads}}}{dt} = k_f(E)\left[1 - \theta_{MH_{ads}}\right] - k_b(E)\,\theta_{MH_{ads}} - k_2\theta_{MH_{ads}} + k_{-2}\left[1 - \theta_{MH_{ads}}\right] \tag{16}$$

$$\frac{d\theta_M}{dt} = -\frac{d\theta_{MH_{ads}}}{dt} \tag{17}$$

The next assumption is that the potential perturbation is slow enough that the measurements are essentially at equilibrium/steady state, so that all along the current trace, at least in the vicinity of $E^{0'}$ the measured $i(E)$ value reflects the equilibrium/steady state concentration.

Apply the steady state approximation to the intermediate $\theta_{MH_{ads}}$.

$$\frac{d\theta_{MH_{ads}}}{dt} = 0 = k_f(E)\left[1 - \theta_{MH_{ads}}\right] - k_b(E)\,\theta_{MH_{ads}} - k_2\theta_{MH_{ads}} + k_{-2}\left[1 - \theta_{MH_{ads}}\right] \tag{18}$$

Solve for $\theta_{MH_{ads}}$.

$$0 = k_f(E)\left[1 - \theta_{MH_{ads}}\right] - k_b(E)\,\theta_{MH_{ads}} - k_2\theta_{MH_{ads}} + k_{-2}\left[1 - \theta_{MH_{ads}}\right] \tag{19}$$

$$= k_f(E) + k_{-2} - \theta_{MH_{ads}} \left[k_f(E) + k_b(E) + k_2 + k_{-2} \right] \tag{20}$$

$$\theta_{MH_{ads}} = \frac{k_f(E) + k_{-2}}{k_f(E) + k_b(E) + k_2 + k_{-2}} \tag{21}$$

From Equation 15,

$$\begin{aligned}
\frac{i(E)}{FA\Gamma^*/\delta} &= k_f(E)\left[1 - \theta_{MH_{ads}}(E)\right] - k_b(E)\,\theta_{MH_{ads}}(E) && (22)\\
&= k_f(E) - \left[k_f(E) + k_b(E)\right]\theta_{MH_{ads}}(E) && (23)\\
&= k_f(E) - \frac{\left[k_f(E) + k_b(E)\right]\left[k_f(E) + k_{-2}\right]}{k_f(E) + k_b(E) + k_2 + k_{-2}} && (24)\\
&= \frac{\begin{array}{c} k_f(E)\left[k_f(E) + k_b(E) + k_2 + k_{-2}\right] \\ -\left[k_f(E) + k_b(E)\right]\left[k_f(E) + k_{-2}\right] \end{array}}{k_f(E) + k_b(E) + k_2 + k_{-2}} && (25)\\
&= \frac{k_f(E)\,k_2 - k_b(E)\,k_{-2}}{k_f(E) + k_b(E) + k_2 + k_{-2}} && (26)
\end{aligned}$$

Rearranging,

$$\begin{aligned}
\frac{i(E)}{FA\Gamma^*/\delta} &= \frac{k_f(E)\,k_2 - k_b(E)\,k_{-2}}{k_f(E) + k_b(E) + k_2 + k_{-2}} && (27)\\
\frac{i(E)}{FA\Gamma^*/\delta}\left[k_f(E) + k_b(E) + k_2 + k_{-2}\right] &= k_f(E)\,k_2 - k_b(E)\,k_{-2} && (28)\\
\frac{i(E)}{FA\Gamma^*/\delta}\left[k_2 + k_{-2}\right] &= k_f(E)\,k_2 - k_b(E)\,k_{-2} && (29)\\
&\quad - \frac{i(E)}{FA\Gamma^*/\delta}\left[k_f(E) + k_b(E)\right] \\
\frac{i(E)}{FA\Gamma^*/\delta}\left[k_2 + k_{-2}\right] &= k_f(E)\left[k_2 - \frac{i(E)}{FA\Gamma^*/\delta}\right] && (30)\\
&\quad - k_b(E)\left[k_{-2} + \frac{i(E)}{FA\Gamma^*/\delta}\right] \\
\frac{i(E)}{k_2 FA\Gamma^*/\delta}\left[1 + \frac{k_{-2}}{k_2}\right] &= k_f(E)\left[1 - \frac{i(E)}{k_2 FA\Gamma^*/\delta}\right] && (31)\\
&\quad - k_b(E)\left[\frac{k_{-2}}{k_2} + \frac{i(E)}{k_2 FA\Gamma^*/\delta}\right]
\end{aligned}$$

Allow, to make the fittings dimensionless,

$$K_2 = \frac{k_{-2}}{k_2} \tag{32}$$

and a scaled measured current

$$I(E) = \frac{i(E)}{k_2 F A \Gamma^* / \delta} \tag{33}$$

such that

$$I(E)[1 + K_2] = k_f(E)[1 - I(E)] - k_b(E)[K_2 + I(E)] \tag{34}$$

Now include the definitions of the forward and backward electron transfer rates, as in Equations 13 and 14. Allow

$$f = \frac{F}{RT} \tag{35}$$

$$\eta = E - E^{0'} \tag{36}$$

The normalized current is now expressed in terms of η.

$$I(\eta)[1 + K_2] = k^0 \exp[-\alpha f \eta][1 - I(\eta)] - k^0 \exp[(1-\alpha) f \eta][K_2 + I(\eta)] \tag{37}$$

Or

$$I(\eta)\frac{[1 + K_2]}{k^0} = \exp[-\alpha f \eta][1 - I(\eta)] - \exp[(1-\alpha) f \eta][K_2 + I(\eta)] \tag{38}$$

3.3.1 Plots of Equation 37

Solve Equation 37 for $I(E)$.

$$I(\eta) = k^0 \frac{\exp[-\alpha f \eta] - \exp[(1-\alpha) f \eta] K_2}{1 + K_2 + k^0 (\exp[-\alpha f \eta] + \exp[(1-\alpha) f \eta])} \tag{39}$$

$$I(\eta) = \frac{\exp[-\alpha f \eta] - \exp[(1-\alpha) f \eta] K_2}{\frac{1+K_2}{k^0} + (\exp[-\alpha f \eta] + \exp[(1-\alpha) f \eta])} \tag{40}$$

Equation 39 can be plotted to illustrated the range of behaviors that might be observed for this model. The inputs that are needed to generate the wave shape $I(\eta)$ as a function of η are the standard heterogeneous electron transfer rate k^0, the ratio of the desorption and absorption rates $K_2 = k_{-2}/k_2$, and the transfer coefficient α. Consider each of the following range of results.

For equal rates of desorption and absorption, $K_2 = 1$ and for a symmetric activation barrier for electron transfer $\alpha = 0.5$, the range of responses for the standard heterogeneous electron transfer rates that are rapid or reversible ($k^0 = 1$ cm/s), quasireversible ($k^0 = 0.1$ cm/s) through slow or irreversible ($k^0 = 0.001$ cm/s) are shown in Figure 12. As is typical for slowing rates of heterogeneous electron transfer, the reductive and oxidative branches shift out symmetrically from $\eta = 0$ as k^0 decreases. The normalized currents limit at +1 and -1 as consistent with a symmetric response .

A similar set of results are shown in Figure except that $K_2 = 0.7$ instead of 1. For $K_2 = 0.7$, the rate of absorption (k_2) is slightly large than the rate of desorption. The result shown in the Figure are similar to those in Figure 12 except the currents limit at 1 for the reduction and about -0.7 for the oxidation. The oxidation step (desorption) is slower than the reduction (absorption) and the relative current is lesser in a ratio that is about the same as the value of K_2.

In Figure 14, Equation 39 is plotted for a slower standard heterogeneous electron transfer rate $k^0 = 0.001$ cm/s, $K_2 = 0.7$, and a four of values of the transfer coefficient, α of 0.6, 0.5, 0.4, and 0.3. The shift in the branches for oxidation and reduction are not symmetric about $\eta = 0$. The reductive branch is steeper relative

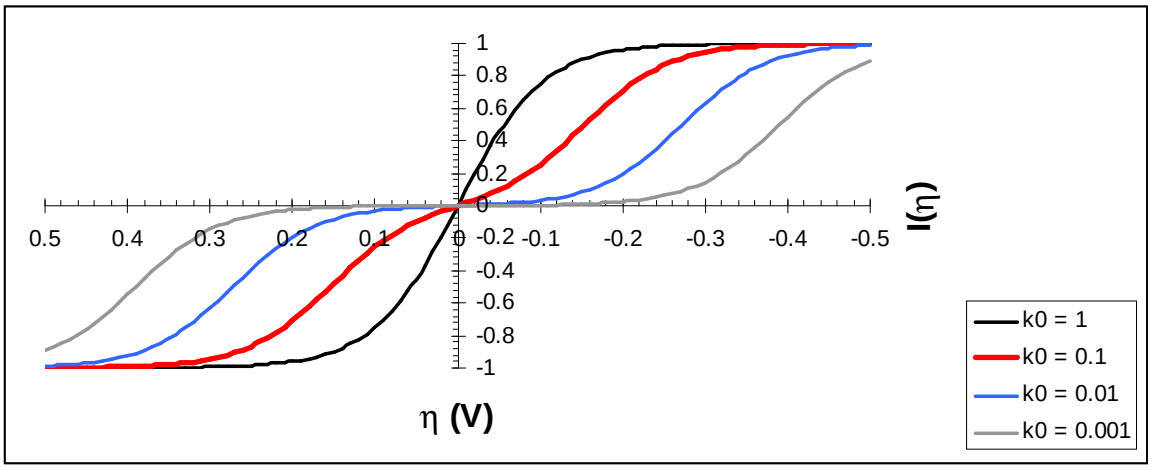

Figure 12. Normalized current $I(\eta)$ as a function of η for equal rates of desorption and absorption, $K_2 = 1$, a symmetric activation barrier for electron transfer $\alpha = 0.5$, and a range of standard heterogeneous rates k^0 of 1.0, 0.1, 0.01, and 0.001 cm/s. The branches for oxidation and reduction shift out symmetrically from $\eta = 0$ and the currents limit at +1 and -1 consistent with the slow electron transfer and symmetric rates of absorption and desorption and symmetric transfer coefficient.

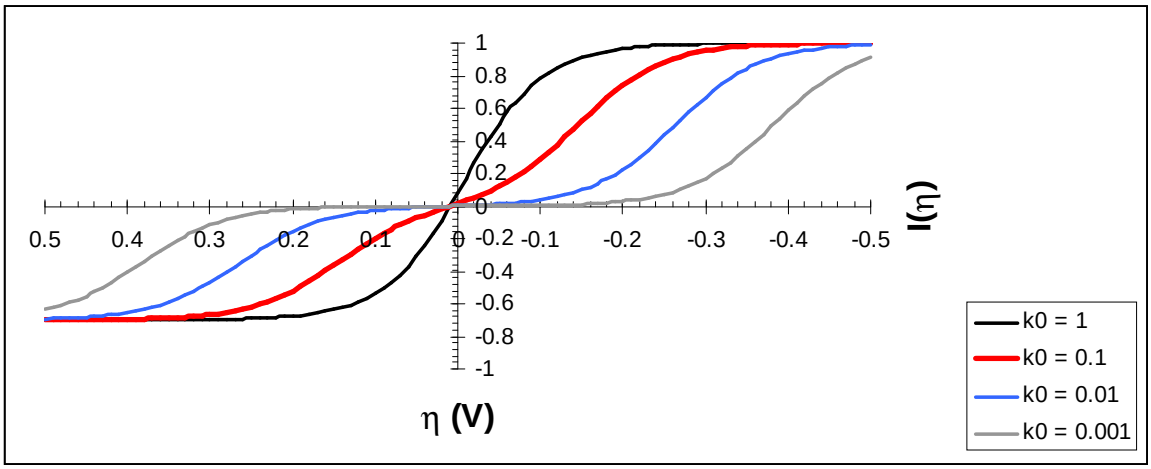

Figure 13. Normalized current $I(\eta)$ versus η for the same conditions in the previous Figure except that $K_2 = k_{-2}/k_2 = 0.7$. Note that with this imput, the normalized current for the slow oxidation step limits at about 70 % of the limiting normalized current for faster reduction step.

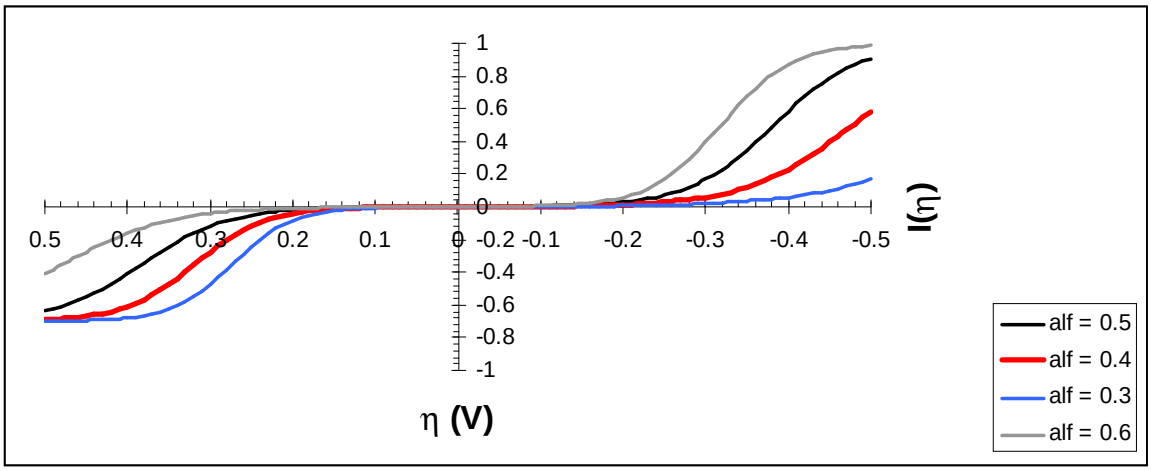

Figure 14. Normalized current $I(\eta)$ versus η for the same conditions of $K_2 = k_{-2}/k_2 = 0.7$ and $k^0 = 0.001$ cm/s and α of 0.6, 0.5, 0.4, and 0.3. As α deviates from the symmetric value of 0.5, the oxidative and reductive branches shift assymmetrically with respect to $\eta = 0$.

to the oxidative branch as α increases. The impacts of K_2 and slow k^0 are consistent with the results above.

Overall, the responses generated from inputs to Equation 39 are consistent with expectation for electron transfer events and the relative limiting values of the normalized currents are consistent with the choice of K_2. The wave shapes generated here are consistent in at least a semi-quantitative manner with the data presented in the thesis. Based on these results, Equation 39 is at least a rough approximation to the mechanism for the hydride formation at palladium. In the next section, Equation 39 is used to approximate the rate constants for the experimental data.

3.3.2 To Approximate the Data

Equation 37 is a near dimensionless fitting expression. To fit the data for a first approximation, make the following initial approximations.

1. $\alpha = 0.5$. This assumes the current potential curves are fairly symmetric.

2. Define $E^{0'}$ as the midpoint between the cathodic and anodic branches on the potential axis. This should be a place to start, especially if the current potential curves are symmetric.

Then Equation 38 is expressed as

$$I(E)\frac{[1+K_2]}{k^0}\exp[0.5f\eta] = [1 - I(E)] - \exp[f\eta][K_2 + I(E)] \tag{41}$$

$$I(E)\left\{\begin{array}{c}\frac{[1+K_2]}{k^0}\exp[0.5f\eta] \\ +1+\exp[f\eta]\end{array}\right\} = 1 - \exp[f\eta]K_2 \tag{42}$$

$$I(E) = \frac{1 - \exp[f\eta]K_2}{\frac{1+K_2}{k^0}\exp[0.5f\eta] + 1 + \exp[f\eta]} \tag{43}$$

The shape of the current curve with potential can then be approximated by adjusting only K_2 and k^0. Once a good fit of shape is found, then k_2 may be approximated from normalization of $I(E)$.

From the experimental data, an estimated approximation for the rate constants was determined. The values corresponding to closest approximation with the experimental data can be seen in Table 6. It can be seen that the use of magnets

Table 6. Rate Parameters Estimated from the Model.

Parameter	**Approximated Value for Blank TMODA**	**Approximated Value for Nonmagnetized C1 Particles**	**Approximated Value for Magnetized Particles**
Alpha	0.07	0.018	0.012
k_0 (cm/s)	1×10^{-8}	1×10^{-3}	1×10^{-3}
k_1 (cm)	1×10^{-4}	1×10^{-4}	1×10^{-4}
k_{-1} $\left(cm^{-1}\right)$	1×10^{-2}	1×10^{-2}	1×10^{-2}
k_2 $\left(cm^{-1}\right)$	1×10^{5}	1×10^{10}	1×10^{10}
k_{-2} (cm)	1×10^{-9}	1×10^{-4}	1×10^{-4}

increases the kinetic rate of absorption and desorption by approximately five orders of magnitude.

The approximation has only attempted to model the absorption process. It is of note that the curve which approximates the absorption process does not readily model the desorption process, suggesting that the mechanism may be different for the absorption process compared to the desorption process.

3.3.3 Case for Small Polarization beyond E^0

In this case, the polarization is sufficiently small that only a small fraction of the sites on the metal surface are blocked as MH_{ads}. The available reaction sites with no adsorbed hydride are sufficiently numerous that the reaction rate is not significantly limited by the few blocked sites.

CHAPTER 4

CONCLUSIONS

4.1 Final Thoughts

With the future of fossil fuel supplies unclear, it is imperative that alternative enery sources be developed to meet the needs of a petroleum dependent economy. Hydrogen promises sustainability and energy efficiency, however, at present the costs associated with a hydrogen fuel system outweigh those of petroleum. Safe and compact storage of hydrogen must be accomplished before it can be recognized as a common fuel source. Metal hydrides demonstrate a relatively stable way in which to store hydrogen, however, the kinetics of absorption and desorption of hydrogen present problems for the time scale required for fuel useage.

This work explored the use of magnetic microparticles in order improve the reaction kinetics of hydrogen absorption and desorption in palladium metal. Magnetic microparticles were shown to effectively decrease potential required to electrochemically drive hydrogen absorption in the metal, thus decreasing the energetic cost associated with such a reaction.These preliminary studies provide proof of concept and offer insight into the reaction kinetics of the palladium hydride system. It is the hope of the author that this work will inspire creative innovation in the way hydrogen storage is studied and developed.

4.2 Future work

This work creates a background for future studies and a scaffold to support further experimental design. The results herein describe achievements within a limited field of the palladium hydrogen system.

The absorption and desorption of hydrogen have been studied at various temperatures and pressures, so future work should examine how the magetic microparticles effect kinetics and current output in a broad temperature range. Since the majority of systems that could be powered by a hydrogen fuel system are operated at temperatures above or below room temperature, more exploration of the temperature effects on the magnetically modified palladium hydride system should be explored. Essentially, the question of whether more hydrogen can be absorbed at higher temperatures or pressures with the use of magnets should be examined. The magnetically modified electrode should readily adapt to these changes in experimental conditions.

The magnetic particles studied herein were of limited field strength due to the contraints of coating requirements. The acidity of the film materials limits the usability of uncoated particles. In future, stronger magnetic microparticles such as $SmCo_5$ or NdFeB could be coated in house or purchased with a coating. The TMODA modified films were only studied with SiMAG microparticles, thus there is room for further exploration of magnetic particle type in TMODA films.The electrochemical properties of Nafion and TMODA are well studied, however future studies may choose to examine other polymers for the film.

The time scale of the CV measurements obtained is much less than the time scale of significant hydride formation. Thus, future work may explore the longer time scale measurements to more accurately depict the amount of hydride formation comparable to that needed for fuel storage.

Many recent studies use palladium particles, films, or even nanotubes in order to get the absorption effect of palladium in a ligther metal material [13]. The use of magnetic microparticles in these applications could be explored to provide broader application of the technology.

Finally, the results show significant gains for the palladium hydrogen system, but the use of isotopes such as deuterium should also be explored.

REFERENCES

[1] Sandi, G. *Interface* **2004,** 40-43.

[2] Jerkiewicz, G. *Progress in Surface Science* **1998,** *57,* 137-186.

[3] Sakintuna, B.; Lamari-Darkrim, F.; Hirscher, M. *International Journal of Hydrogen Energy* **2007,** *32,* 1121-1140.

[4] Graham, T. *Proceedings of the Royal Society of London* **1867,** *16,* 422-427.

[5] Flanagan, T. B. *Annu. Rev. Mater. Sci.* **1991,** 269-304.

[6] Bard, A.; Faulkner, L. *Electrochemical Methods;* John Wiley Sons, Inc.: New York, Second ed.; 2001.

[7] Grden, M.; Lukaszewski, M.; Jerkiewicz, G.; Czerwinski, A. *Electrochimica Acta* **2008,** *53,* 7583-7598.

[8] Lee, H. C. *Magnetic Field Effects on Electron Transfer Reactions: Heterogeneous Photochemical Hydrogen Evolution and Homogenous Self-Exchange Reaction,* Thesis,.

[9] Zook, L. A.; Leddy, J. *Anal. Chem.* **1996,** *68,* 3793-3796.

[10] Minteer, S. D. *Magnetic Field Effects on Electron Transfer Reactions,* Ph.D. thesis, University of Iowa, 2000, 2000.

[11] Klotzbach, T.; Watt, M.; Ansari, Y.; Minteer, S. *J. Membrane Sci.* **2006,** 276-283.

[12] Lasia, A.; Gregoire, D. *J. Electrochem. Soc.* **1995,** *142,* 3393-3399.

[13] Lipson, A. G.; Lyakhov, B. F.; Saunin, E. I.; Solodkova, L. N.; Tsivadze, A. Y. *International Journal of Hydrogen Energy 37,* 5676-5685.